Geophysical Research Letters

Supporting Information for

Indonesian Throughflow drove Australian climate from humid Pliocene to arid Pleistocene

B.A. Christensen[1]*, W. Renema[2], J. Henderiks[3], D. De Vleeschouwer[4], J. Groeneveld[4], I.S. Castañeda[5], L. Reuning[6], K. Bogus[7], G. Auer[8], T. Ishiwa[9], C.M. McHugh[10], S.J. Gallagher[11], C.S. Fulthorpe[12], and Expedition 356 Scientists[13]

[1]Environmental Studies Program, Adelphi University, 1 South Avenue, Garden City NY, 11530, USA. [2] Naturalis Biodiversity Center PO Box 9517, Leiden 2300 RA, the Netherlands. [3]Department of Earth Sciences, Uppsala University, Villavägen 16, Uppsala 75236, Sweden. [4]MARUM–Center for Marine and Environmental Sciences and Department of Geosciences, University of Bremen, 28359 Bremen, Germany. [5]Department of Geosciences, University of Massachusetts at Amherst, Amherst MA 01003, USA. [6]EMR – Energy and Mineral Resources Group, Geological Institute, RWTH, Aachen University, Wuellnerstrasse, Aachen 52056, Germany. [7]International Ocean Discovery Program, Texas A&M University 1000, Discovery Drive, College Station, TX 77845-9547 USA. [8]Institute of Earth Sciences, University of Graz, Heinrichstrasse 26, Graz 8010, Austria. [9]Atmosphere and Ocean Research Institute, University of Tokyo, 5-1-5 Kashiwanoha, Kashiwa-shi, Chiba 277-8564, Japan. [10]School of Earth and Environmental Sciences, Queens College (C.U.N.Y.), 65-30 Kissena Blvd. Flushing NY 11367, USA. [11]School of Earth Sciences, University of Melbourne, Melbourne, Victoria 3010, Australia. [12]Institute for Geophysics, University of Texas, Austin, 10100 Burnet Road (R2200), Austin TX 78758-4445, USA.

Contents of this file

Introduction

This supporting information provides further background on modern Australian climate and Indian Ocean circulation (Text S1 and Figure S1), the age model for Site U1463 (biostratigraphic datums; Figure S4; Table S1), enhanced explanations of our methods and justification for our climatic interpretations of Site U1463 wireline logs (Text S2 and Figures S2-S3, S5-8; Table S2), organic geochemistry data for Site U1463 (Text S3, Figure S10 and Table S3) as well as additional supporting data for Australian Neogene paleoclimate and vegetation changes (Text S4; Figure S9). The wireline logs and biostratigraphic data presented in this paper were collected on International Ocean Discovery Program (IODP) Expedition 356 during August and September 2015. Supporting XRD analyses were conducted at Aachen University. Organic geochemical analyses were performed at University of Massachusetts, Amherst.

Text S1. The modern Australian Monsoon and Indian Ocean Circulation

Today, the northern Australian continent receives moisture delivered by the monsoon with the rainfall maximum occurring in January (austral summer) [*Nicholson*, 2011] and a strong monsoon is present north of 25°S from December to March [*Herold et al.,* 2011; *Suppiah*, 1992] (Figure S1). The monsoon is associated with moist west to northwesterly flow, which originates in the Indian Ocean and waters of southern Asia [*CSIRO*, 2015]. Monsoon rains tend to be sporadic and associated with localized convective thunderstorms, but prolonged rainfall can occur when coupled with the Intertropical Convergence Zone (ITCZ) [*Nicholson*, 2011]. As Australia has little topographic variability, especially in the interior, seasonal heating pulls the ITCZ far inland and sets up monsoonal rain linked to the Asian system. The dominant winds in Northern Australia reverse seasonally, with summer northerly or westerly monsoonal flow, contrasting with southerly trades prevailing in the winter in northern and central regions of the Australian continent [*Nicholson*, 2011] ; Figure S1c,d). Overall, the southeasterly trades, which occur for >11 months in central Australia and 9-11 months in many parts of northern Australia, are the dominant wind system [*Nicholson*, 2011]. Climate change is altering modern temperature and rainfall intensity patterns [*CSIRO*, 2015].

Reorganization of the position and intensity of ocean gateways directly impacts Indian Ocean circulation [*Molnar and Cronin*, 2015; *Schott et al*., 2009]. The modern ITF sets up the East Gyral Current (EGC) (Figure 1) and therefore controls modern equatorial Indian Ocean circulation [*Gordon*, 2005]. Both the EGC and the ITF supply relatively fresh and warm water that forms the Leeuwin Current through eastward gyre flow [*Schott et al*., 2009]. The Leeuwin Current in turn limits the influence of the cool northward-flowing West Australia Eastern Boundary Current [*Nicholson*, 2011]. Similarly timed changes throughout the Indian Ocean [*Karas et al*., 2011, 2009, 2011] (Figure 4) have indicated a major reorganization of its circulation that is linked to changes in the ITF, which flows through the tectonically active Maritime Continent (MC).

Text S2. Foundations for Climatic Interpretation of Site U1463

S2.1 Clay mineralogy

The relative content of clay mineral phases (illite, kaolinite) in seventeen bulk samples was analyzed using X-ray diffraction (XRD) to ground-truth the wireline logs (Table S2). Bulk sediment samples were freeze-dried and ground by hand, top-mounted onto a sample holder and analyzed using a Bruker ASX D-4 Endeavor X-ray Diffractometer mounted with a Vantec-1 detector using nickel-filtered CuKα radiation. All samples were scanned at 40 kV/40 mA, from 4°–70° with a step size of 0.0087°2θ and a speed of 0.2 s/step. The external corundum standard NIST 176 was measured periodically to monitor data quality. Diffractograms were evaluated using the DIFFRACplus EVA software package, after baseline removal. Peak heights and I/Icorundum values from the International Centre for Diffraction Data PDF database were used to measure the relative abundance of all mineral phases.

S2.2 Wireline Logs

The biostratigraphic age model (Figure S4) provides the foundation for the tuning of the wireline logs. Shipboard micropaleontological analyses were based on core catcher samples (10-20 m resolution) in Holes U1463B and C. The biostratigraphic datums are calibrated to the geological timescale of *Gradstein* [2012]. They were highly consistent between both holes and were combined into one age-depth model (Table S1).

Potassium (K) has previously been used as a proxy for fluvial runoff offshore NW Australia (see main text). The covariation of clay mineral abundance (mainly illite) with K (Figure S5a) confirms this relationship for Site U1463. Illite and other clay minerals are commonly measured in river waters in the study area [*Gingele and De Deckker*, 2004; *Gingele et al*., 2001; *Gingele et al*., 2001b = 84]. Therefore we use K% as an indicator of continental moisture.

The Th/K ratio at Site U1463 records changes in mineral assemblages. Eolian sediments from the northwest dust trajectory of Australia are known to be enriched in heavy minerals [*Kuhnt et al*., 2015; *Stuut et al*., 2014]. Heavy minerals are rich in Th and commonly accumulate in soils and are transported in wind-blown dust [*Calvert and Peterson*, 2007]. Although the Th/K ratio has been related to both changes in the kaolinite/illite ratio [*Hesselbo*, 1996] and the concentration of heavy minerals [*Simicek and Bàbek*, 2015], the kaolinite/ illite ratio for our site is essentially flat despite variations in Th/K (Figure S5e). We therefore interpret higher Th/K ratios at our study as increased heavy mineral content from wind blown dust.

We propose the use of U ppm as an additional proxy for dust transport in our study area. U ppm is not a traditional proxy for eolian transport, but the strong correlation with our eolian indicators suggests U ppm is a robust additional proxy. Dust is transported to our study area via the modern dust pathway [*Bowler*, 1976] (Figure 1a) from an area that contains U-rich surface igneous rocks [*Schofield*, 2009] providing a direct source for the uranium at U1463. Additionally the uranium content is typically high in heavy minerals, such as zircon [*O'Hara et al*., 2001; *Svendsen and Hartley*, 2001], and the eolian fraction offshore NW Australia is enriched in Zr [*Kuhnt et al*., 2015; *Stuut et al*., 2014]. Finally, a significant increase in average U concentration occurs after 2.4 Ma (t-test, unequal variance; $t=29.02$, $df=1066$, $p<0.0001$); the increase persists in flux measurements (Figure S5c), indicating that the variation is not a productivity or dilution signal. The increase in U (ppm), concurrent with increased variability in Th/K and reduction in clay mineral abundance, supports our interpretations of long-term climate change in NW Australia. The surface radiogenic maps of Australia [*Nakamura and Milligan,* 2015] support our interpretations. Surface measurements of % K are greater in areas around the rivers (Gascoyne, Ashburton, Fortescue, De Grey, Fitzroy; Fig. S6) that supply our study area. Furthermore, Th/K and U ppm are elevated under the modern dust pathway (Figures S7, S8). The radiometric map of Australia [*Nakamura and Milligan*, 2015] indicates relative abundance of U ppm and Th/K is not uniform under the dust pathway and supports variation between the two records downcore.

Text S3. Organic Geochemistry at Site U1463

S3.1 Alkenones and TEX_{86}

The organic geochemistry of 18 samples from Site U1463 were analyzed postcruise at the Biogeochemistry Laboratory at the University of Massachusetts Amherst on an aliquot of the squeezecake sediment left over from shipboard interstitial water (IW) sampling. Interstitial water samples were obtained by squeezing 5 or 10 cm whole-round sections cut from cores. Before squeezing, the exterior of the whole-round sample was carefully cleaned with a spatula to remove potential contamination by drilling fluid. For extended core barrel (XCB) cores, the intruded drilling mud between biscuits was also removed to eliminate contamination from drilling fluid. The cleaned sediment was placed into a 9 cm diameter titanium squeezer that was then placed in a Carver hydraulic press [*Manheim and Sayles*, 1974] and squeezed at pressures no higher than 25,000 lb (~17 MPa) to prevent the release of interlayer water from clay minerals. The squeezed interstitial water was collected for shipboard geochemistry analyses while a portion of the leftover sediment residue was freeze dried for 24 hours, homogenized with a mortar and pestle, and analyzed for total carbon (TC), total nitrogen (TN) and total inorganic carbon (TIC). These samples were stored at 4°C until analysis.

The samples were freeze dried at the University of Massachusetts Amherst and subsequently homogenized with a mortar and pestle prior to lipid extraction. A total lipid extract (TLE) was obtained by extraction with 9:1 dichloromethane (DCM)/methanol (v/v) using an Accelerated Solvent Extractor (ASE 200). Each TLE was further separated into apolar, ketone and polar fractions using alumina oxide column chromatography with solvent mixtures of 9:1 hexane/DCM (v/v), 1:1 hexane/DCM (v/v), and 1:1 DCM/methanol (v/v), respectively.
The ketone fractions were analyzed on an Agilent 7890 gas chromatograph equipped with two flame ionization detectors (GC-FID) and two Agilent 7693 autosamplers. 5 % phenyl methyl siloxane columns (HP-5, 60 m x 0.32 mm x 0.25 µm) were used. The oven program ramped from 70°C to 130°C at a rate of 20°C min^{-1}, then from 130°C to 320°C at a rate of 4°C min^{-1}, and held at the final temperature for 20 min. The concentration of individual compounds was determined via external calibration curves of squalene ranging in concentration from 1 ng/µl to 100 ng/µl for each FID. Compounds were identified by a Hewlett Packard 6890 gas chromatograph coupled to an Agilent 5973 Mass Selective Detector equipped with a 5 % phenyl methyl siloxane column (HP-5MS 60 m x 0.25 mm x 0.25 µm), with an identical oven program to the GC-FID.

The polar fractions were dissolved in a mixture of 99:1(v/v) hexane/isopropanol and filtered through a 0.45 µm PFTE filter before being analyzed by high performance liquid chromatography mass-spectrometry (HPLC-MS) for glycerol dialkyl glycerol tetraethers (GDGTs) [*Hopmans et al*., 2000; *Schouten et al*., 2002]). Samples were analyzed on an Agilent 1260 series HPLC coupled to an Agilent 6120 MSD using a Prevail Cyano column (150 mm x 2.1 mm, 3 µm) and 99:1 hexane:propanol (vol:vol) as the eluent. After 5 minutes, the eluent increased by a linear gradient up to 1.8 % isopropanol (vol) over the next 45 min at a flow rate of 0.2 mL min^{-1}. Scanning was performed in single ion monitoring (SIM) mode.

TEX_{86} ratios were calculated as described by *Schouten et al.*, [2002] and the BAYSPAR calibration [*Tiernery and Tingley*, 2014] was applied (Table S3; Figures 4 and S10). BIT Index values [*Kim et al*. 2010] were low ranging from 0.11 to 0.35 (Table S3).

S3.2 Organic Geochemistry Results and Discussion

The ketone fractions were analyzed for alkenones to investigate use of the $U^{k'}_{37}$ Index at site U1463. No alkenones were detected in the three oldest samples (>4.87 Ma; below 355 m depth CSF-A). Unfortunately, a compound co-eluting with the $C_{37:3}$ alkenone was present in nearly all samples thereby precluding use of the $U^{k'}_{37}$ Index as SST proxy without further separation of the ketone fraction, which may be possible using a different type of column [*Longo et al*., 2013]. Here we use concentrations of the much larger $C_{37:2}$ alkenone peak, normalized to TOC, as a productivity proxy. No compounds co-eluted with the $C_{37:2}$ alkenone.

GDGTs were found to be abundant in all samples analyzed and were used to reconstruct SST using the TEX_{86} proxy [*Schouten et al.*, 2002]. We note that TEX_{86} is calibrated to SST using global surface sediments; however, at the present the global calibration datasets does not include any samples from the Northwest Australian Shelf [*Tiernery and Tingley*, 2015]. For this reason we caution against interpreting absolute TEX_{86} temperatures although trends are robust.

Overall, the TEX_{86} record, albeit it at low resolution, suggests somewhat similar timing between changes in SST and major changes in conditions on the Australian continent. Generally higher SSTs are noted during the Australian Humid Interval while lower SST is noted during the Arid Interval (Figure S10). While upwelling could be a possible explanation for the drop in TEX_{86} SSTs from 2.3 to 0.76 Ma, alkenone concentrations, which provide a proxy for primary production, do not increase at this time. Instead, alkenone abundances fluctuate throughout the record but do not exhibit any clear patterns with the TEX_{86} record (Figure S10). Thus, it appears that the drop is SST is not related to upwelling. We conclude that TEX_{86} likely reflects SST and the lower temperatures noted after ~2.7 Ma (in the interval from 2.3 to 0.76 Ma) played a role in driving the transition from the humid to the arid conditions on the Australian continent (Figure S10).

Text S4. Previous studies of Australian Neogene paleoclimate and vegetation

A summary of previous studies of Australian climate from the late Miocene to Pleistocene is presented graphically in Figures 3 and S9. Much work has been done in this region, but many of the records are distant from the study area (the circle is 1500 km in radius), and focused on the southeast [*Martin*, 2006; *Kershaw et al*., 1994; *Macphail*, 1997], relying on outcrops representing only brief stratigraphic intervals. This is due to numerous factors, such as a lack of thick onshore deposits from intense erosion/weathering [*Martin*, 2006; *Macphail*, 1997; *Hill*, 2004; *Macphail*, 2007; *Byrne et al*., 2008], the selective oxidation of direct vegetation evidence (i.e., pollen and spores), particularly in central and northwestern Australia [*Macphail*, 1997], and complex offshore transport (e.g., eolian vs. fluvial [*Martin and McMinn*, 1994) and deposition histories that can be further complicated by sea level changes [*Martin*, 2006] and reworking (e.g., turbidites [*Martin and McMinn*, 1994]).

Originally, it was thought that southern Australia experienced persistent aridity since the late Miocene [*Bowler*, 1982], but other studies have challenged this [*Kershaw* et al., 1994]. A recent study found woody taxa (e.g., *Gyrostemonaceae*, *Casuarinaceae*, *Haloragaceae*) indicating semi-arid conditions transitioning to vegetation (mesic) more indicative of wetter conditions into the early Pliocene [*Sniderman et al*., 2016]. This is in agreement with palynological evidence offshore northwestern Australia (ODP Site 765) [*Martin and McMinn*, 1994] that indicates relatively higher moisture (compared to the late Pliocene and later) in the late Miocene-early Pliocene, shown by the dominance of *Casuarinaceae*, interpreted to form forests based on the lower abundance of herbaceous taxa such as *Restionaceae* and *Gyrostemonaceae*, and very low counts of grass pollen (*Poaceae*). The one unequivocal rainforest taxon, *Nothofagus*, is absent despite being found at similar times in southwestern, southeastern and northeastern Australia [*Bint*, 1981; *Martin and McMinn*, 1993; *Dodson and Ramrath*, 2011]. The similarity between ODP Site 765 pollen assemblages [*Martin and McMinn*, 1994] and a well-dated and robust reconstruction in southern Australia [*Sniderman et al*., 2016], combined with similar paleobotanical evidence from southwestern [*Chen and Barton*, 1991], southeastern [*Martin*, 2006] and offshore northeastern [*Martin and McMinn*, 1993] Australia, paleotemperature [*Quilty*, 1994] (Figure 3) and paleoprecipitation information [*Metzger and Retallack*, 2010; *Sniderman* et al., 2016] (Figure 3) suggest that the early Pliocene was warmer and wetter than today, consistent with our Humid Interval. Our well-dated record fills a data gap in northwestern Australia and thus contributes strong evidence that wetter conditions prevailed around the entire periphery of Australia during the latest Miocene-early Pliocene.

Between the early and late Pliocene, there was a progression from a relatively more humid environment to a drier environment, coincident with our Transitional Interval. Also during this time, it has been suggested [*Macphail*, 20o7] that west-east environmental gradients were established. For example, vegetation differences between southwestern and southeastern Australia were not as significant as previously supposed in the early Pliocene, and regional differences developed from the late Pliocene [*Bint*, 1981] with the contraction of the mesic biome [*Byrne et a*l., 2011]. Desertification in the Simpson Desert has been dated to begin between 4-2 Ma [*Fujioka et al*., 2005] and most arid zone biotic lineages date to at least the Pliocene [*Byrne et al*., 2008] In the palynological record off northwestern Australia (Site 765), *Poaceae* increased rapidly in abundance from the early to late Pliocene, and the palynological record is from then dominated by *Poaceae*, *Chenopodiaceae* and *Asteraceae* with minor *Acacia* and *Myrtaceae* [*Martin and McMinn*, 1994]. In southeastern Australia, vegetation is successively replaced by drought- and fire-tolerant sclerophyll, a process that is complete by the early Pleistocene [*Kershaw et al.,* 1994 *Sniderman et al*., 2007]. In southwestern Australia, there are aridity events dated between 2.9 and 2.56 Ma [*Dodson and Macphail*, 1994]. All of these continent-wide changes around this interval suggest a major climate transition, but detailed information about its nature and timing have been difficult to constrain [*Kershaw et al*., 1994; *Macphail*, 1997; *Sniderman*, 2011; *Sniderman et al*., 2013].

Evidence for truly arid conditions can be found from direct dating arid landforms, suggesting that the heightened aridification began in central Australia before expanding outwards in the Pleistocene with desertification intensifying after 1 Ma [*Fujioka et al*., 2009]. In northwestern Australia, the casuarinaceous forests had been replaced by grasslands by the late Pleistocene where the presence of *Chenopodiaceae*/*Amaranthaceae* could also have indicated an arid landscape [*Martin and McMinn*, 1994]. This is consistent with paleolake studies of the middle Pleistocene

[*Chen and Barton*, 1991; *McLaren and Wallace*, 2010] and a pollen record from southern Australia that shows an assemblage similar to the modern *Chenopodiaceae*-dominated shrubland by the middle Pleistocene [*Sniderman* et al., 2016]. The rate of intraspecific diversification of arid zone biota also seems to have increased in the Pleistocene [*Byrne et al*., 2008]. All of this evidence points towards another profound shift in Australian climate. Thus, our record identifying the onset of aridity at 2.3 Ma adds to these previous records and provides a well-constrained and unique, particularly for northwestern Australia, point with which to more holistically evaluate climatic changes around continental Australia during the late Neogene.

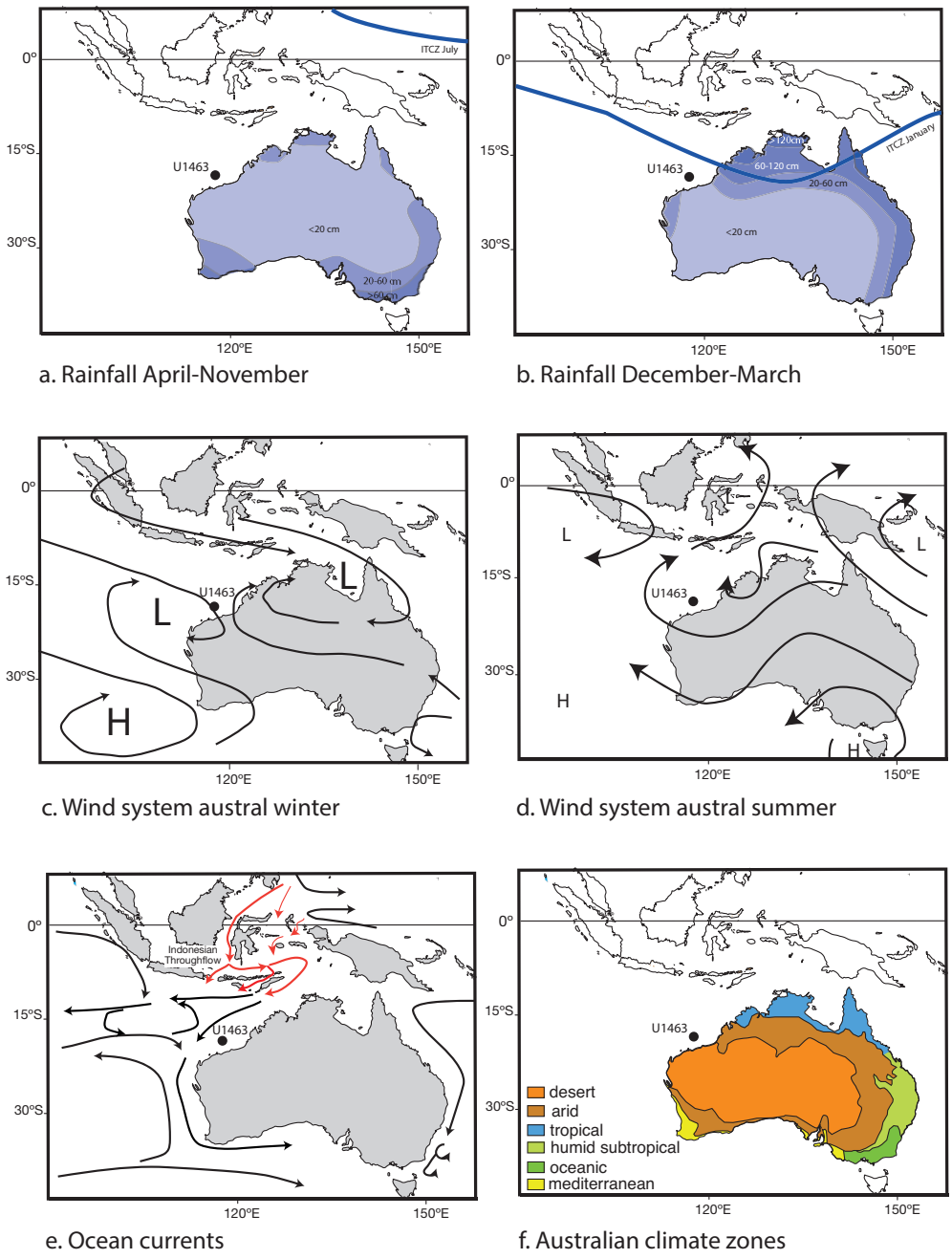

Figure S1. Modern Australian climate and ocean circulation [*Nicholson*, 2011]. Rainfall and ITCZ position in (a) austral winter and (b) summer. Wind patterns in (c) austral winter and (d) summer. Arrows show predominant wind directions. L: low pressure area, H: high pressure area. (e) Ocean circulation around the Maritime Continent and Australia. Arrows indicate the main current systems [*Schott et al.*, 2009]. The Indonesian Throughflow is marked in red. (f) Modern Australian climatic zones.

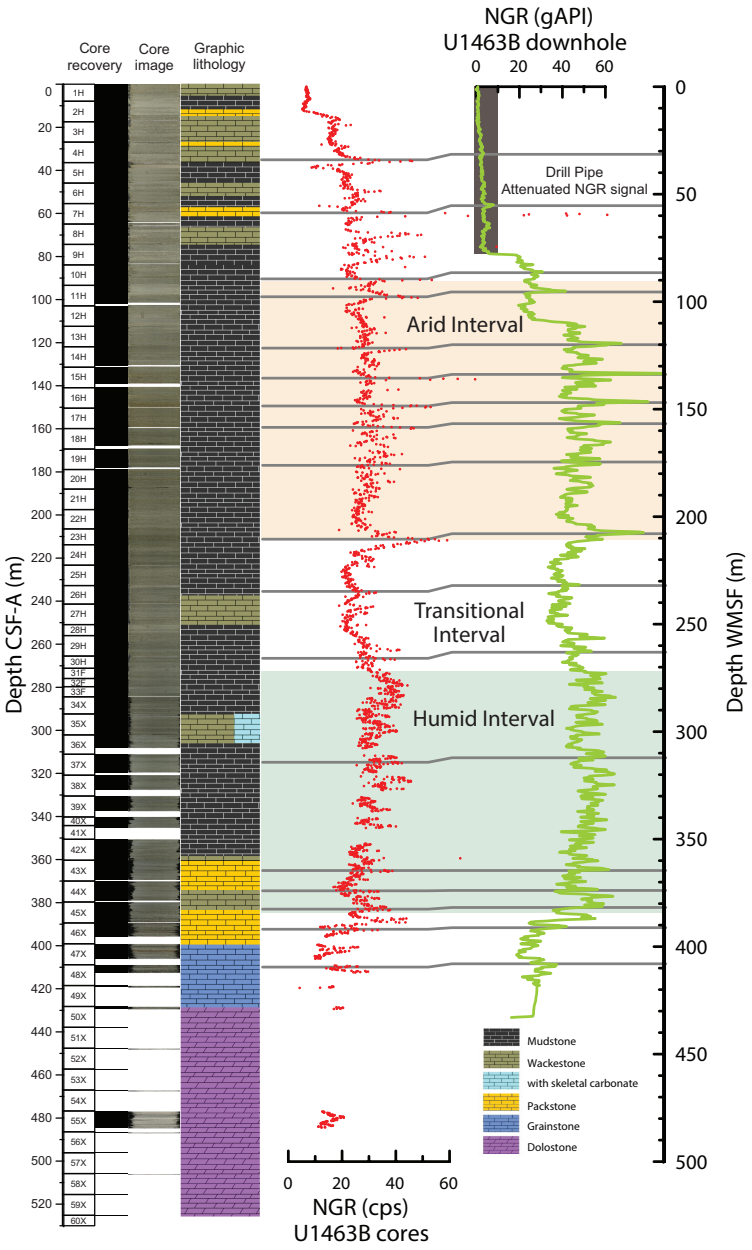

Figure S2. Lithostratigraphy, core recovery and total gamma radiation (NGR) measured on cores of Hole U1463B (left). This information is core-based and uses the CSF-A depth scale. Total NGR measured during downhole logging (right) uses the WMSF depth scale. The relation between both depth scales was determined by the correlation of distinctive features in core-based and wireline NGR. Biostratigraphic datums and other core-based information used in this study were converted from the CSF-A to the WMSF depth scale by linear interpolation between these tiepoints.

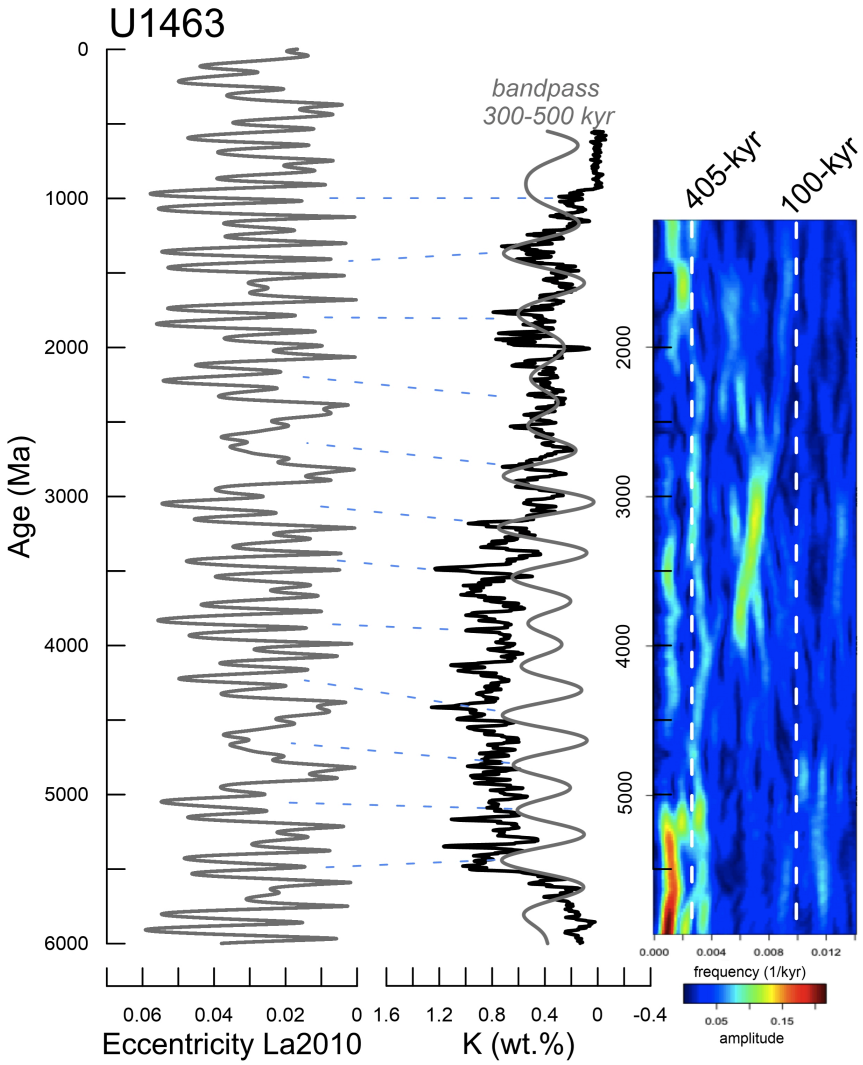

Figure S3. Evolutive harmonic analysis (1200 kyr windows) of wireline K logs from Site U1463 along the biostratigraphic age model. The 300-500 kyr bandpass filtered signal was tuned to the 405-kyr cycles in the La2010 eccentricity solution [*Laskar et al.*, 2011].

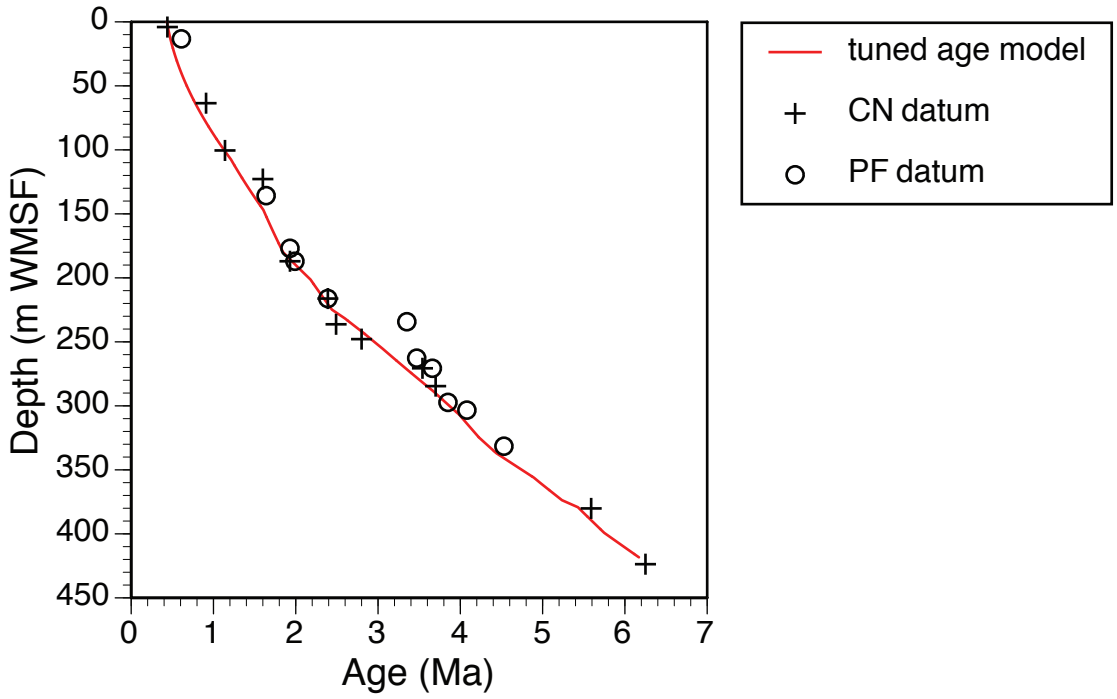

Figure S4. Age-depth relationship of Site U1463. The age model was derived from cyclostratigraphic tuning of the wireline K logs (red line; see also Figure S3) and biostratigraphic datums as given in Table S1 (symbols). Crosses indicate calcareous nannofossil (CN) and circles depict planktonic foraminifer (PF) datums.

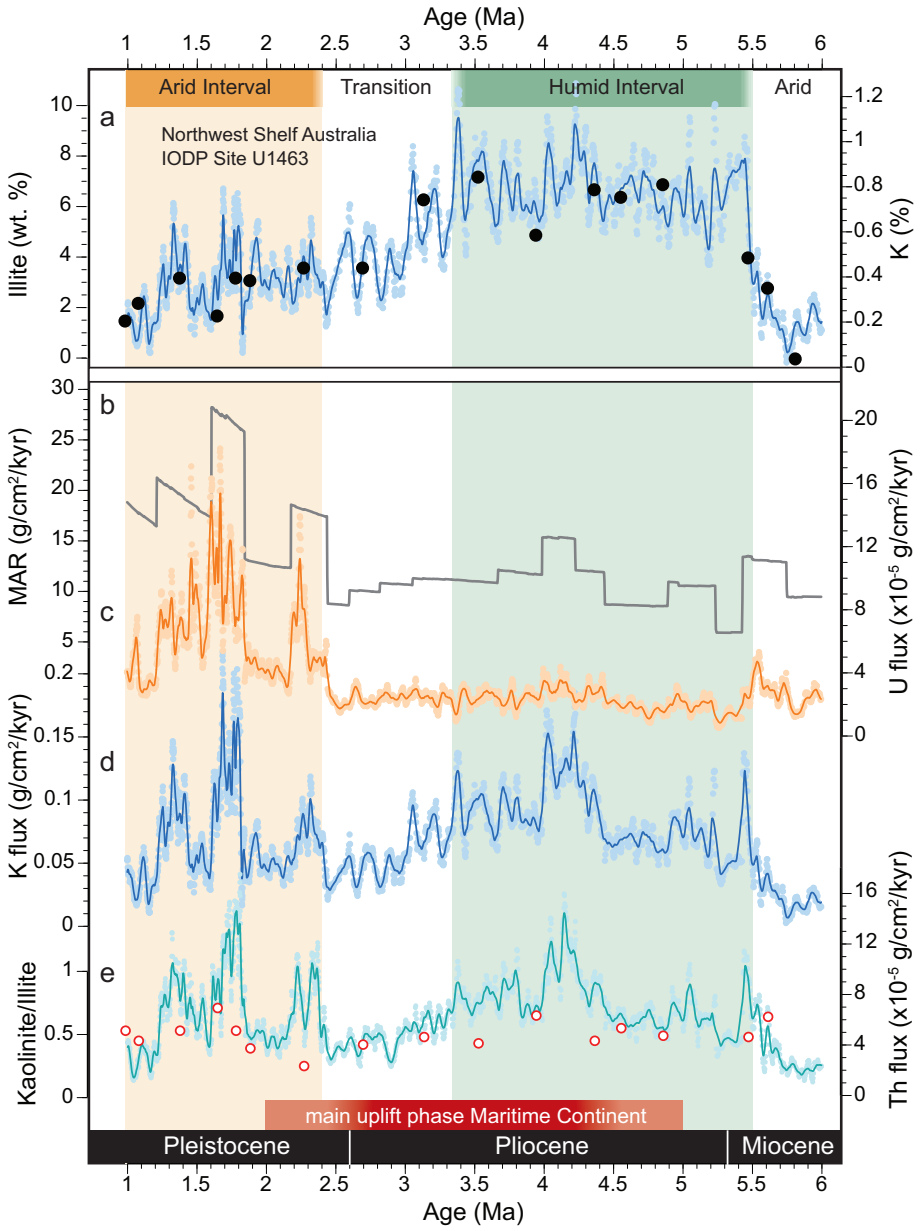

Figure S5. Downhole wireline log data compared to clay mineralogy from discrete sediment analyses (a) and mass accumulation rates at Site U1463 (b-e). (a) Potassium (K, %) log overlain with XRD illite abundance estimates (black dots; wt. %). (b) Bulk sediment mass accumulation rates (g/cm^2/kyr), used to calculate elemental fluxes of (c) Uranium (10^{-5} g/cm^2/kyr), (d) Potassium (g/cm^2/kyr) and (e) Th (10^{-5} g/cm^2/kyr) overlain with kaolinite/illite ratio (red circles; unitless). A 15-point moving average is applied to records in a,c,d,e. The Humid Interval (~5.5–3.3 Ma), Transitional Interval (3.3–2.4 Ma) and the Arid Interval (2.4 Ma onward) are indicated. Uplift in the Maritime Continent (MC), controlling flow through the ITF, is highlighted in red with the strongest colors keyed to most likely timing.

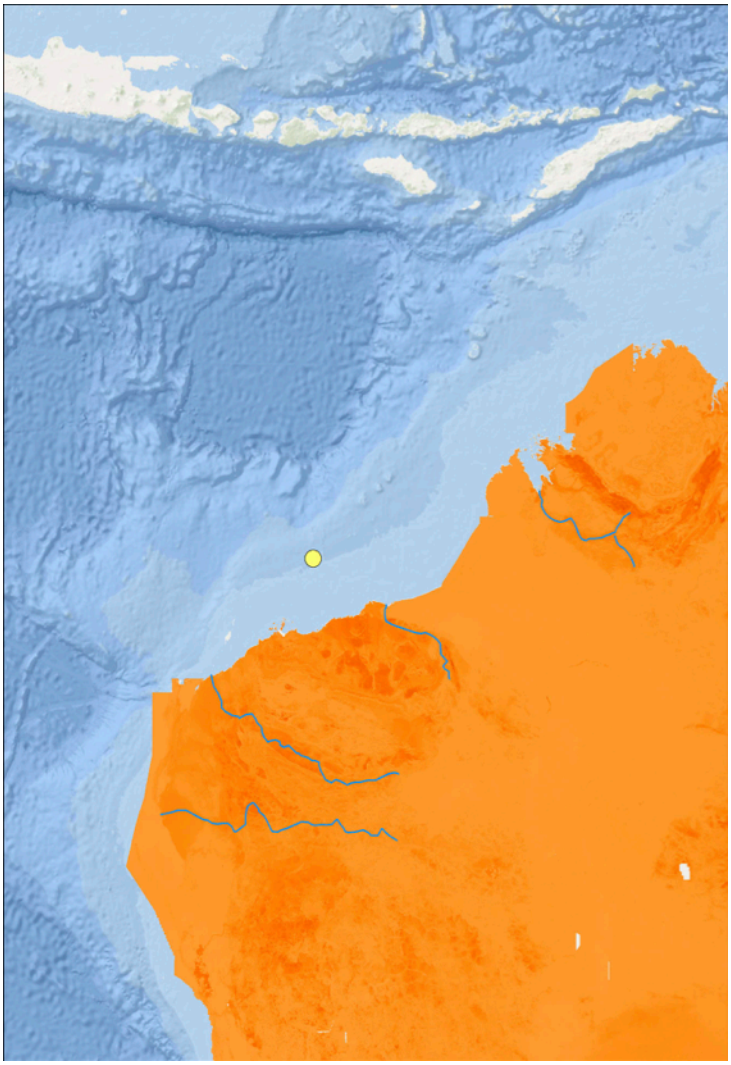

Figure S6 Map of distribution of %K at surface, Northwest Australia. Radiometric surface data are from continental radmap v3 2015 unfiltered pct potassium grid [*Geosciences Australia,* 2015]. Darker orange indicates presence, lighter orange absence. Map scale 1:12,500,000.

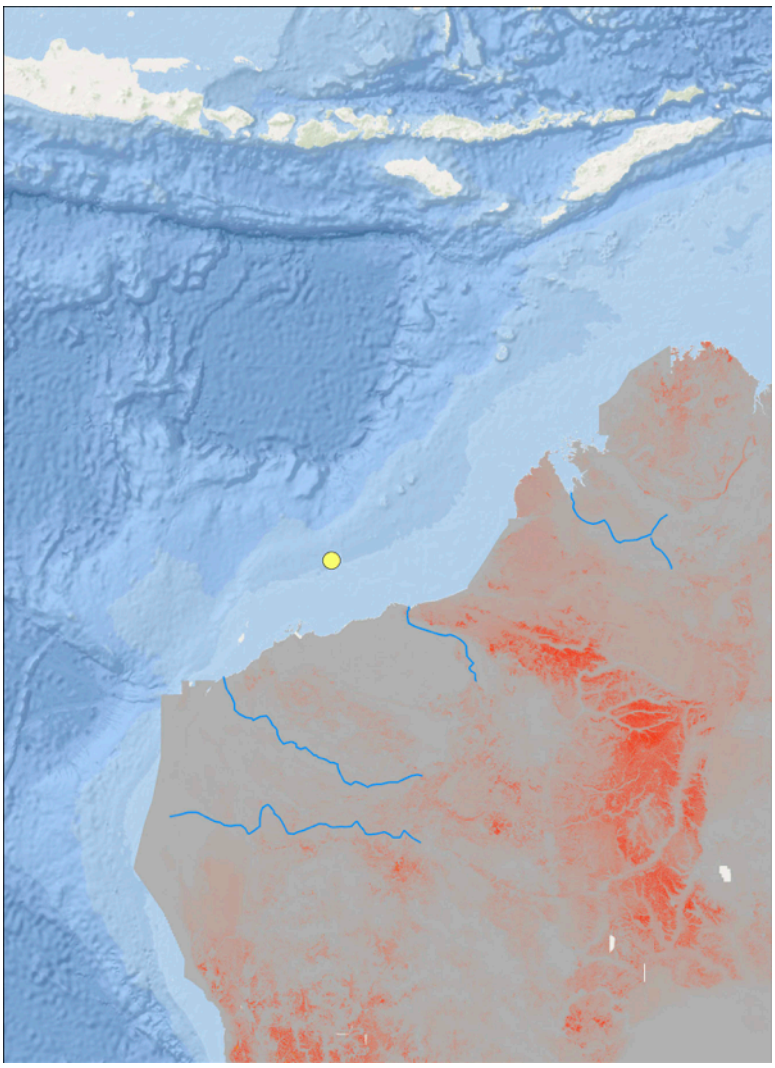

Figure S7. Map of distribution of Th/K at surface, Northwest Australia. Radiometric surface data are from and continental radmap v3 2015 ratio thorium over potassium grid [*Geosciences Australia,* 2015] . Dark red indicates presence, lack of red indicates absence. Map scale 1:12,500,000.

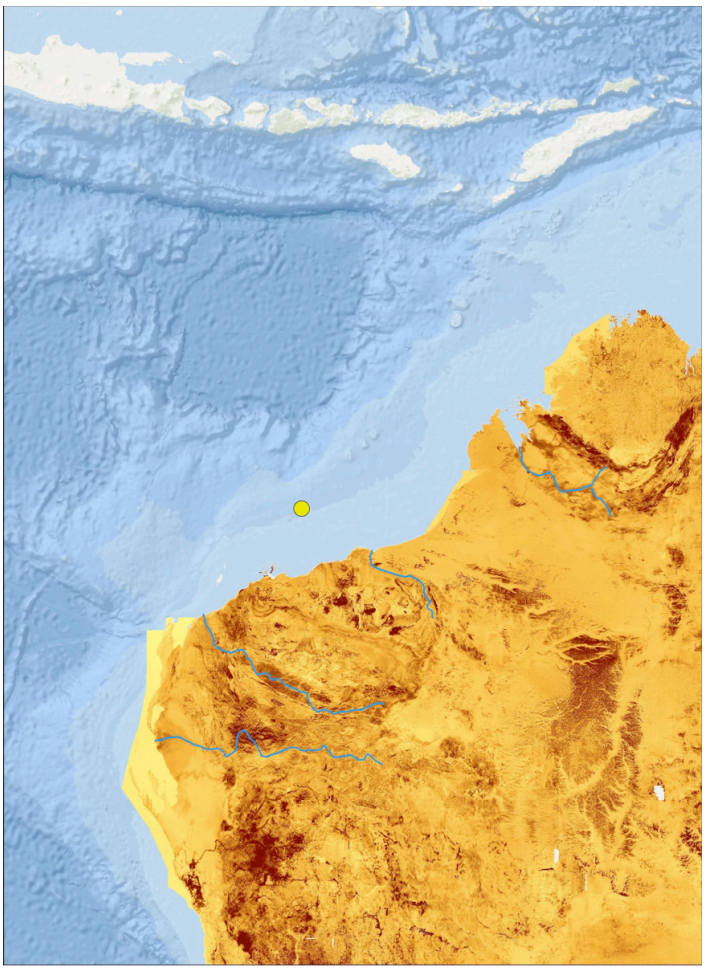

Figure S8. Map of distribution of Uppm at surface, Northwest Australia. Radiometric surface data are from continental radmap v3 2015 [*Geosciences Australia,* 2015] . Dark brown indicates increased presence, light tan indicates low levels to absence. Map scale 1:12,500,000.

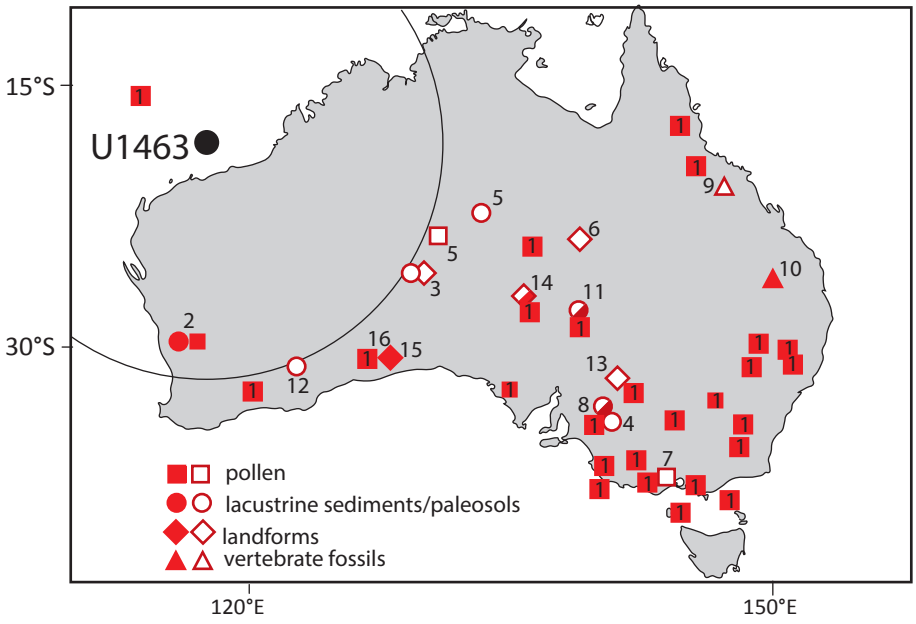

Figure S9. Compilation of records used to evaluate late Neogene Australia paleoclimate. The numbers correspond to the following studies in the References and Supplemental references: (1) Sites reviewed in *Kershaw et al.* [1994], *Macphail* [1997] and *Martin* [2006]; (2) *Dodson and Ramrath* [2001], *Dodson and Macphail* [2004]; (3) *Chen and Barton* [1991]; (4) *Zhisheng et al.* [1986]; (5) *English et al.* [2001]; (6) *Fujioka et al.* [2009]; (7) *Sniderman et al.* [2007]; (8) *McLaren and Wallace* [2010]; (9) *Hocknull et al.* [2007]; (10) *Montanari et al.* [2013]; (11) *Bowler* [1982], *Metzger and Retallack* [2010]; (12) *Zheng et al.* [1998]; (13) *Fujioka and Chappell* [2010]; (14) *Fujioka et al.* [2005]; (15) *Miller et al.* [2012]; (16) *Sniderman et al.* [2016].

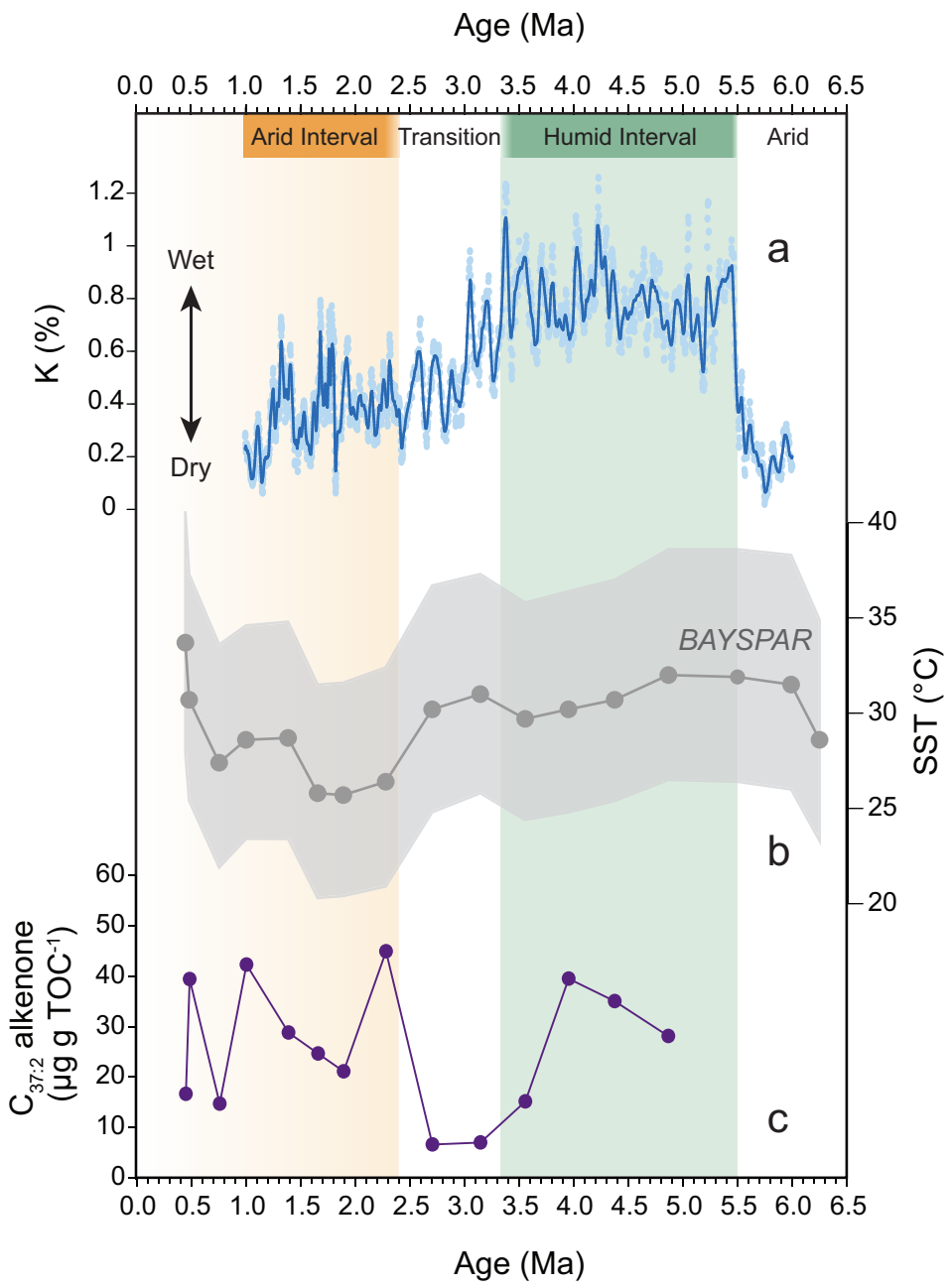

Figure S10. Organic geochemistry data at Site U1463 compared to wireline log climate proxy. (a) Site U1463 K% indicating relatively wet and dry intervals (see Figure 2 caption, main text). (b) Site U1463 GDGT data plotted using the BAYSPAR calibration of *Tierney and Tingley* [2014]. The median BAYSPAR value is plotted and the shaded area represents the 5th and 95th percentiles. (c) Concentrations of the $C_{37:2}$ alkenone normalized to TOC.

Depth (m CSF-A)	Depth (m WMSF)	Marker species	Type	Age (Ma)	Reference
4.11	4.06	Top *P. lacunosa*	CN	0.44	1
13.45	13.30	Top *G. tosaensis*	PF	0.61	1
64.54	63.55	Top *R. asanoi*	CN	0.91	1
101.89	100.48	Base *R. asanoi*	CN	1.14	1
125.12	122.82	Top *C. macintyrei*	CN	1.60	1
139.28	135.79	Top *G. apertura*	PF	1.64	1
182.24	176.92	Base *G. truncatulinoides*	PF	1.93	1
192.05	187.03	Top *D. brouweri*	CN	1.93	1
192.05	187.03	Top *G. extremus*	PF	1.99	1
220.54	216.19	Top *D. pentaradiatus*	CN	2.39	1
220.54	216.19	Top *G. limbata*	PF	2.39	1
238.89	234.28	Base *G. tosaensis*	PF	3.35	1
240.7	236.27	Top *D. surculus*	CN	2.49	1
251.26	247.87	Top *D. tamalis*	CN	2.80	1
265.63	262.74	Top *D. altispira* (Pacific)	PF	3.47	1
273.88	270.65	Top *Sphenolithus* spp.	CN	3.54	1
273.88	270.65	Top *P. primalis*	PF	3.66	1
288.41	284.58	Top *R. pseudoumbilicus* (>7 μm)	CN	3.70	1
301.75	297.30	Top *G. margaritae*	PF	3.85	1
308.11	303.34	X *Pulleniatina* sin to dex	PF	4.08	1
334.71	331.52	Top *S. kochi*	PF	4.53	1
386.22	380.13	Top *D. quinqueramus*	CN	5.59	1
412.44	409.81	Top *R. rotaria*	CN	6.25	2

Table S1. Biostratigraphic datums used for the U1463 age model in Figure 3. CN: Calcareous nannofossils, PF: Planktonic foraminifers. References: 1. *Gradstein et al.* [2012]; 2. *Young* [1998].

CSF-A (m)	Kaolinite	Illite	Kaolinite/Illite
52.62	1.3	1.4	0.9
87.60	0.8	1.5	0.6
96.77	1.0	2.2	0.5
126.30	1.7	3.2	0.5
154.80	1.2	1.7	0.7
173.1	1.7	3.2	0.5
183.28	1.2	3.1	0.4
210.9	0.9	3.6	0.3
237.2	1.5	3.6	0.4
260.4	3.0	6.3	0.5
282.61	3.1	7.2	0.4
305	3.2	4.9	0.7
333.4	3.0	6.7	0.4
342.41	3.5	6.4	0.6
355.00	3.4	6.9	0.5
383.78	1.9	4.0	0.5
391.58	1.8	2.8	0.7
402.6	2.1	0.0	
479.01	0.0	0.0	
486.59	0.0	0.0	

Table S2. Clay mineralogy. Illite, kaolinite and the ratio of kaolinite to illite.

site	core	depth	depth (CSF-A)	est Age Ma	TEX86	BIT Index	TEX^{H}_{86} T°C	BAYSPAR T°C (5^{th})	BAYSPAR T°C (50^{th})	BAYSPAR T°C (95^{th})
U1463	1H4	145-150	5.95	0.45148	0.774	0.12	30.98	27.9	33.7	40.6
U1463	4H4	145-150	15.65	0.48601	0.727	0.11	29.13	25.4	30.7	37.3
U1463	7H4	145-150	61.35	0.76052	0.673	0.17	26.85	21.9	27.4	33.6
U1463	10H3	145-150	88.35	1.0054	0.692	0.24	27.66	23.4	28.6	34.6
U1463	14H3	140-150	126.3	1.3904	0.694	0.16	27.73	23.4	28.7	34.8
U1463	17H3	140-150	154.8	1.6608	0.646	0.31	25.63	20.3	25.8	31.5
U1463	20H3	140-150	183.28	1.8955	0.645	0.31	25.60	20.4	25.7	31.6
U1463	23H3	140-150	210.9	2.2835	0.656	0.35	26.07	20.9	26.4	32.4
U1463	26H3	140-150	237.2	2.7083	0.718	0.25	28.76	24.8	30.2	36.7
U1463	29H3	140-150	260.4	3.1477	0.732	0.21	29.34	25.8	31.0	37.3
U1463	33F2	141-151	282.61	3.55825	0.709	0.33	28.37	24.4	29.7	35.8
U1463	36X2	140-150	305	3.95445	0.717	0.16	28.72	24.8	30.2	36.4
U1463	39X2	140-150	333.4	4.3766	0.727	0.17	29.13	25.4	30.7	37.0
U1463	42X3	140-150	355	4.86795	0.747	0.15	29.92	26.5	32.0	38.6
U1463	45X3	126-136	383.78	5.5002	0.745	0.12	29.85	26.4	31.9	38.6
U1463	48X1	136-146	410.16	5.99005	0.740	0.14	29.65	26.0	31.5	38.3
U1463	55X5	89-99	483.48	>6.25	0.693	0.34	27.70	23.3	28.6	34.9

Table S3. TEX_{86} data for Site U1463. TEX^{H}_{86} is calculated from *Hopmans et al.* [2000] and BAYSPAR TEX_{86} temperature estimates are calculated from *Schouten et al.* [2002]. Note that the age of the lowermost sample at 483.38m CSF-A is currently unknown; the closest biostratigraphic datum at 412.44 m (Table S1) yields an age of 6.25 Ma.